

An Exploration of Remote Sensing Methods Using EUMETSAT Data

Richard Vaughan and Greg Wilkinson
(F34IMP Image and Image Processing)
(Dated: November 10, 2017)

Remote Sensing methods can yield a wide array of information about the earth and its atmosphere. By processing this information, it is possible to extract both qualitative and quantitative data describing vegetation, snow and other ground level features. Here, we demonstrate several methods of cloud removal required to extract useful information about surface level features. We then calculate the Normalised Difference Vegetation Index (NDVI), and observe its seasonal fluctuation in Central Africa. We found that the NDVI in a specific region of Central Africa varied approximately sinusoidally in 2011.

I. INTRODUCTION

Remote Sensing methods involve using radiation measurements in specific spectral bands to observe and infer the state of certain regions of the atmosphere, without coming into physical contact with them [1]. When remote sensing the Earth's surface, spectral bands are selected for which the atmosphere is most transparent. Measurements in the visible and near-infrared ranges of the electromagnetic spectrum are of particular relevance for surface observation, as different types of terrain absorb and reflect radiation in these bands in different proportions [1][2].

Remote Sensing methods can be used to observe clouds, surface vegetation, sea surface temperature and atmospheric moisture, for instance. The resulting data has a huge range of applications. Remote sensing offers vital insight into monitoring climate change, weather, droughts, floods and virtually anything that depends directly on the earth's atmosphere; these insights can have huge humanitarian impact [1][3].

The data processed in this report is sourced from EUMETSAT (*European Organisation for the Exploitation of Meteorological Satellites*) - an intergovernmental organisation founded to establish, maintain and exploit European systems of operational meteorological satellites [4]. The spectral band measurements used were collected by the Meteosat-8 geostationary satellite [5]. Data was obtained via a direct downlink with EUMETSAT, in greyscale .jpg format (using equipment which the University of Nottingham has recently acquired).

In this report, we outline various techniques for performing quantitative analysis of satellite images of the Earth. We perform simple cloud detection and removal, determine vegetation density and snow coverage using established remote sensing techniques and measure spatial and temporal variation in vegetation in a region of Central Africa.

II. CLOUD REMOVAL METHODS

Cloud Removal is imperative in achieving quantitative analysis of ground level features in satellite images. In this section, we present a number of different meth-

ods which lessen the visual impact of clouds on satellite images. The methods presented rely on a data set of the order of 100 images, acquired on different dates. This is because it is necessary to observe fluctuations in pixel value over time to determine whether they correspond to clouds or not.

For the purposes of explaining cloud removal, this section is concerned entirely with the visible $0.6\mu\text{m}$ band, for simplicity. The data featured in this section were acquired at 12:00pm ± 5 mins every day between 10/03/2012 and 15/06/2012 (86 days total), these data will hereon be referred to as the *2012 Data Set*. It is important to note that for the visible $0.6\mu\text{m}$ band clouds correspond to bright pixel values; this is not the case for all bands (e.g. the infrared $8.7\mu\text{m}$ band).

It is self-explanatory that applying an ideal cloud removal method should return the image as though there had been no clouds present in the first place. However, it is crucial to preserve the fidelity of the data also. Therefore the efficacy of a cloud removal technique is not determined purely by whether the clouds are removed, but also by its effect on cloudless pixels.

Fig. 1 shows four example images of the earth acquired in the visible $0.6\mu\text{m}$ band.

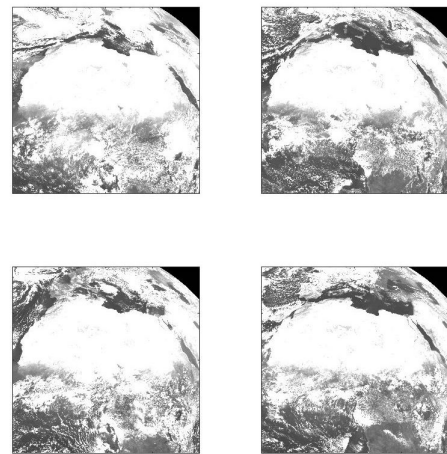


FIG. 1. Four images of North Africa acquired in the visible $0.6\mu\text{m}$ band. The four images correspond to four randomly selected dates in 2012 between March and June. Resolution = 2000 x 2000.

It is clear to see in Fig. 1 that clouds effectively obscure ground level features. It also demonstrates the extent to which clouds typically cover the region of North Africa. Note that cloud pixels appear to have very similar pixel values to the Sahara Desert due to the similar radiance of water vapour and sand, illustrating the need for cloud removal in these satellite images.

In our investigation, the most basic technique employed to remove clouds was to average the images over time. The second technique we employed involved defining a global threshold below which there are no clouds, and then averaging those values. The third technique was simply to take the minimum values of the pixels over time. The fourth, and most complex technique, involved averaging the pixel values which were less than 1σ above the mean value over time, for that pixel. The results of applying these techniques are displayed in Fig. 2.

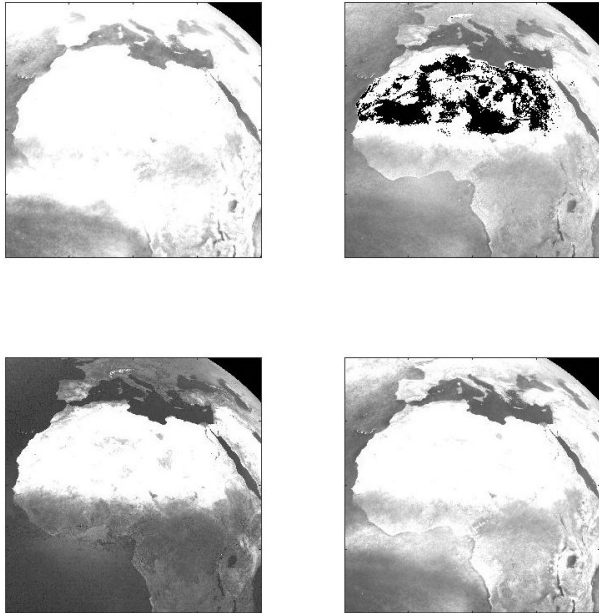


FIG. 2. Images resulting from four different methods of calculating a cloudless image using the *2012 Data Set*. Top Left: Mean image. Top Right: Mean of globally thresholded images. Bottom Left: Minimisation image. Bottom Right: Average pixel values less than 1σ above the mean value over time, for that pixel.

The images presented in Fig. 2 allow for qualitative comparison between the four different techniques. To enable more quantitative comparison, histograms were calculated for each of the images. These histograms are presented in Fig. 3

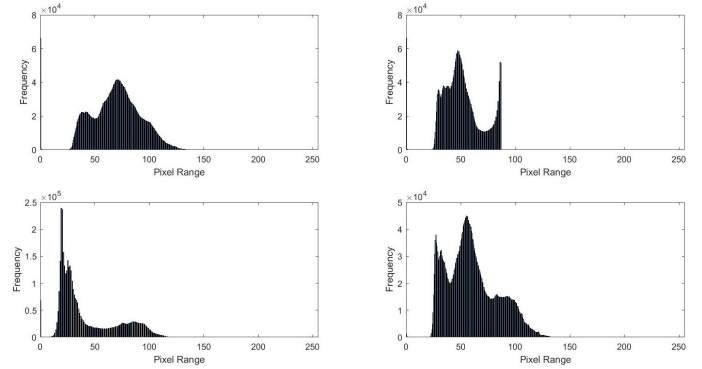


FIG. 3. Histograms of the pixel values resulting from four different methods of calculating a cloudless image using the *2012 Data Set*. Top Left: Mean image. Top Right: Mean of globally thresholded images. Bottom Left: Minimisation image. Bottom Right: Mean pixel values below one standard deviation above the mean.

By considering the information presented in Figs. 2 and 3, we can begin to assess the validity of the four methods.

The simple averaging method has the advantages of being computationally inexpensive, conceptually simple and it requires no user input (threshold values etc.). However, averaging does not completely remove clouds; it effectively dilutes the presence of the clouds, which is not ideal.

Averaging the globally thresholded image pixel values is very problematic. This problem is evident in the top right subset of Fig. 2, the black pixels in the middle of the Sahara Desert correspond to *NaN* values (calculation error). These *NaN* values occur as a result of the way in which the threshold is implemented. The cloud threshold value of greylevel 88 (determined by eye using a simple bespoke thresholding tool provided in the supplementary material) is actually brighter than the centre of the Sahara Desert. Therefore when we calculate the averages, we are in fact dividing by zero at those pixel locations. Raising the threshold value to greylevel 120, which is brighter than all of the desert, eliminates this problem and results in an image containing no *NaN* values. However, the threshold is then inclusive of cloud pixels, which defeats the object of cloud removal. This effect can also be inferred from the top right subset of Fig. 3; it is evident because the histogram abruptly ends at the bin corresponding to the threshold value of greylevel 88. Effectively, this technique is capping the data at a pixel value of 88 and this results in information loss in the brightest desert pixels.

The minimisations method (see bottom left subset of Fig. 2) is very effective at cloud removal. This is because the clouds appear brightly and therefore have no effect on a pixel's value, unless it is cloudy at that pixel for the entire year. However, this method is not without flaws; despite this method neglecting all 'brighter noise', it is very susceptible to 'darker noise', because it essentially only considers one data point per pixel.

The fourth method (see the bottom right subset of Fig. 2) is a compromise between the previous two methods. It maintains higher contrast over land mass than the minimisation method, however does not remove clouds as effectively as the minimisation method.

Due to the only partial success of the second and fourth methods, a new method was implemented which involved averaging the images according to a variable threshold. The variable threshold used was the mean image of the *2012 Data Set* (the top left image in Fig. 2). The result of averaging according to a mean threshold image is displayed in Fig. 4.

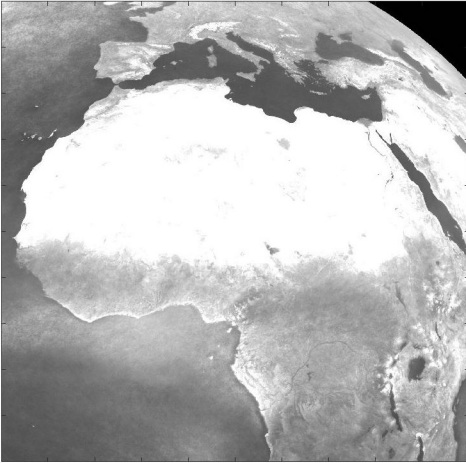


FIG. 4. The result of averaging according to a mean threshold image of the *2012 Data Set*.

By considering the advantages and disadvantages of the five methods discussed above over both land mass and water, it became clear that a composite method was necessary to achieve optimal cloud removal. The two methods used in the composition were the minimisation method, and the averaging according to a mean threshold image method, over water and land respectively. The composition was achieved by masking the results of two methods using a binary land mask available on the EUMETSAT website [4]. The EUMETSAT Land mask is displayed in Fig. 5.



FIG. 5. EUMETSAT land mask binary image.

The resulting composite image is displayed in Fig. 6.

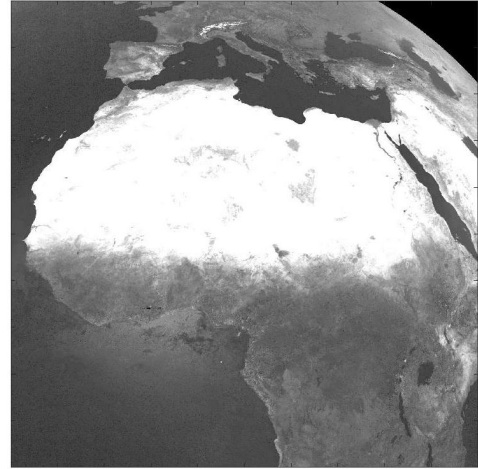


FIG. 6. Composite cloud removed image.

III. PRODUCING A CLOUD FREE COLOUR IMAGE

By applying the composite cloud removal method, outlined in section II, to different spectral bands, it is possible to assemble an RGB colour image. Assembling colour images from different bands is a useful process in satellite observation. Constructing a colour image from cloud removed images of different bands, enables us to qualitatively assess the efficacy of the composite cloud removal method.

The bands chosen to assemble our cloud free colour image are red: $0.6\mu\text{m}$, green: $0.8\mu\text{m}$ and blue: $1.6\mu\text{m}$. These bands were chosen because out of the twelve available bands provided by EUMETSAT, these three are closest to the visible spectrum of light. The ordering of the bands (R,G,B) was determined partly by trial and error, and partly by comparing with the *Meteosat 0 degree*

RGB Composites Natural Colour convention, provided on the EUMETSAT website [4]. An example of a *Meteosat 0 degree RGB Composites Natural Colour* image is displayed in Fig. 7.

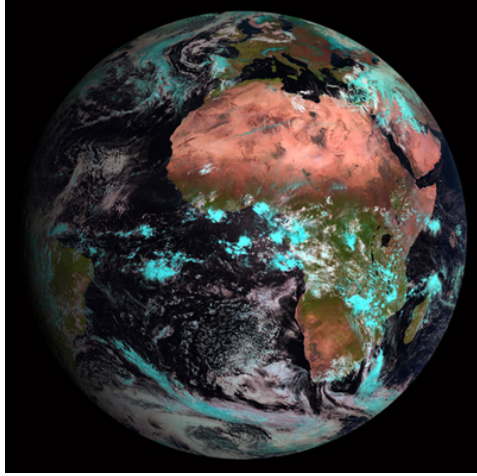


FIG. 7. An example of a *Meteosat 0 degree RGB Composites Natural Colour* image.

The intensity of each channel in our colour image was varied until it most resembled the exemplar image given in Fig. 7. The intensities of the values in each channel were scaled using linear factors. These factors differed for pixels corresponding to land or water (as specified by the land-mask displayed in Fig. 5). The linear factors used to scale the channels are presented in Table I.

	Land	Ocean
R	1.000	1.259
G	0.756	5.259
B	0.378	10.00

TABLE I. Table of linear scaling values for each channel over land and ocean.

Note here that the scaling factors for the ocean pixels are all larger than the scaling factors for the land. This is because during cloud removal the ocean pixels were minimised over time, which makes them systematically darker than in reality. Therefore, larger scaling factors are necessary in order to reverse the signal loss caused by minimisation. The resulting images for each of the three channels are displayed in Fig. 8.

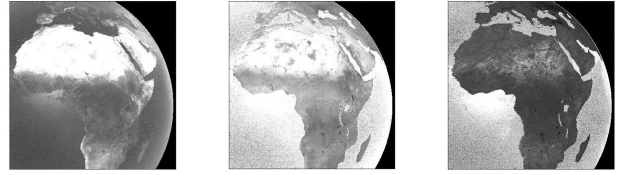


FIG. 8. Scaled images of the red (left), green (centre) and blue (right) channels.

There are several features worth noting in Fig. 8. The red channel is most intense over sandy regions, such as the Sahara Desert, Somalia and the Arabian Peninsula; the green channel is intense over both ocean and sandy regions; whereas the blue channel is generally dark over all land pixels, and generally bright over all water pixels. The combined image (containing the three channels displayed in Fig. 8) is presented in Fig. 9.

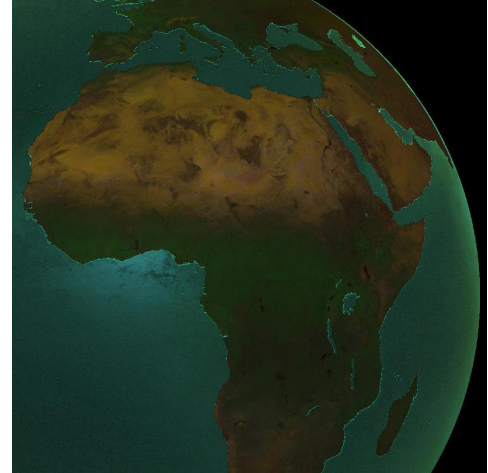


FIG. 9. Combination of the three scaled channels to form a true-colour image

Our colour image resembles the exemplar image shown in Fig. 7. The key difference between the colours in the two images is that the coast lines appear a very bright blue in our image. In order to lessen this effect, it was important to locate the pixels which are at the edges between water and land.

Numerous methods exist to isolate edges in images; because the land-mask is a binary image, we implemented boundary fitting. Boundary fitting involves subtracting the eroded version of an image from the original image. Applying boundary fitting to the land-mask resulted in a binary image corresponding to edge pixels only, which is displayed in Fig. 10.

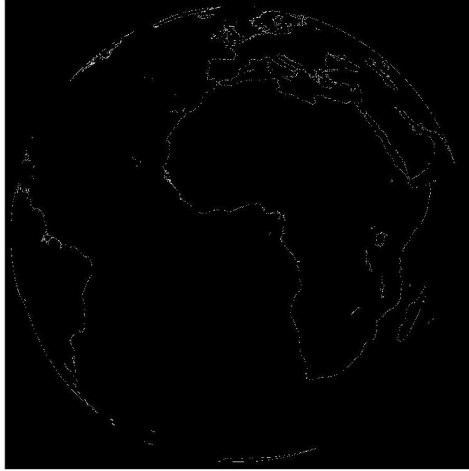


FIG. 10. Boundary fitted image of the land-mask displayed in Fig. 5. Please note that because this image has a resolution of $3712 * 3712$ that the gaps are not actually present.

It is then a trivial operation to set any pixel which corresponds to an edge, to be black in the colour image. The result of setting the edge pixels to be black is displayed in Fig. 11.

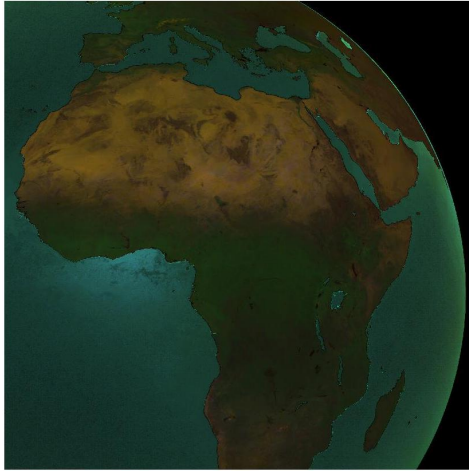


FIG. 11. Composite image using the red, green and blue channels, where coastal pixels are coloured black.

Setting the edge pixels to be black has mostly concealed the bright blue coastal pixels. This final colour image is now more similar in appearance to the exemplar image shown in Fig. 7. This similarity validates the methodology used in sections II and III.

IV. DETERMINING VEGETATION DENSITY AND SNOW COVERAGE

A. The Normalized Difference Vegetation Index

Calculating the Normalized Difference Vegetation Index (NDVI) of a cloud-removed image allows the density of ‘green’ in any given area to be determined.

Visible light (with wavelengths between roughly $0.4\mu m$ and $0.7\mu m$) is absorbed by chlorophyll during photosynthesis. However, near-infrared light (with wavelengths roughly between $0.7\mu m$ and $1.1\mu m$) is strongly reflected by the cell-structure of plant leaves. Hence, the greater the ratio of reflected radiation in the near-infrared band to that in the visible band, the more vegetation within that pixel [2]. Likewise, a lower ratio would indicate that the pixel in question contains less vegetation, barren soil, or desert.

To quantify vegetation density mathematically, the following difference formula is commonly applied:

$$NDVI = \frac{R_{NIR} - R_{VIS}}{R_{NIR} + R_{VIS}}. \quad (1)$$

where R is the physical radiance in either the near-infrared or visible band [1].

However, in order to convert between the binary pixel values extracted from the EUMETSAT images and the physical radiances in Eq. 1, each pixel value must be modified according to calibration constants that are defined for each spectral band [6]. Therefore, R is first calculated as

$$R = CAL_{offset} + CAL_{slope} * PixelValue, \quad (2)$$

for a given band, before applying equation 1. Here CAL_{offset} is the offset constant between each pixel and the physical radiance, with units of $mWm^{-2}sr^{-1}(cm^{-1})^{-1}$, and CAL_{slope} is the linear calibration coefficient, with units of $mWm^{-2}sr^{-1}(cm^{-1})^{-1}$.

The NDVI calculations performed in this project used images in $0.6\mu m$ visible and $8.7\mu m$ spectral bands (shown in Fig. 12). The relevant calibration values were extracted from the headers of the image files. An example NDVI is shown in Fig. 13.

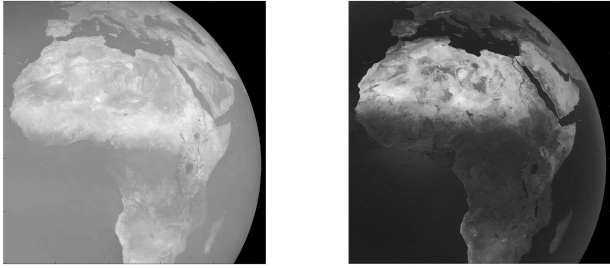


FIG. 12. An example of two images used to calculate the NDVI: one in the $8.7\mu\text{m}$ IR band (left) and another in the $0.6\mu\text{m}$ visible band (right). These images were produced using the cloud removal techniques described in section II, from an initial set of 86 images acquired between March and June 2012.

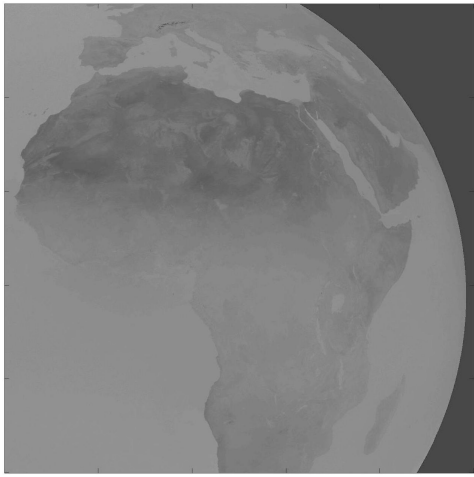


FIG. 13. The calculated NDVI over Africa/Europe, between March and June 2012.

The application of an abrupt thresholding technique such as binarisation to the NDVI provides a quick and rough verification that vegetation density is being detected correctly. Fig. 14 shows a representation of the NDVI where all pixels with an index value of less than 1 are displayed white and all above 1 are displayed black.

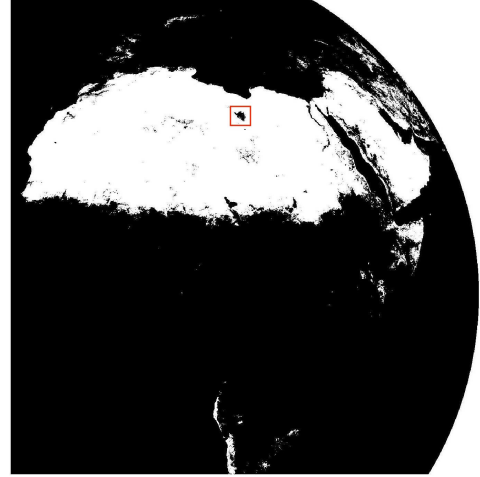


FIG. 14. Binarised NDVI image highlighting barren terrain in white, and showing an unexpectedly dark region of pixels enclosed by a red square.

Black pixels correspond, generally, to vegetation and white areas to more barren soil or desert. The Sahara desert (Northern Africa) for instance is clearly shown in white, whereas the Nile river and its delta (North East Africa) appear black, as expected, due to its lush banks. There is an unexpectedly coloured patch of land, however, in the Northern Central Sahara (enclosed in Fig. 14 by a red box) which appears black although it is amongst barren terrain. This is not vegetation, but the Haruj volcanic field in Libya, comprised of jet black layers of basalt which absorbs light in a manner closer to vegetation than to desert [7][8]. The crude binarised image here correctly identifies the Haruj field as *not* desert, but does not distinguish between basalt, forest and ocean.

The approach taken to generate an NDVI image that ‘makes sense’ aesthetically is to produce a custom colourmap that colours all NDVI pixels below a low threshold brown (representing desert); colours all NDVI pixels above a high threshold green (representing dense rainforest); and creates a linear colour gradient between these two thresholds (to represent indeterminate terrain such as the Haruj volcanic field). After applying the land mask shown in Fig. 5 to discount the ocean pixels, the result is shown in Fig. 15.

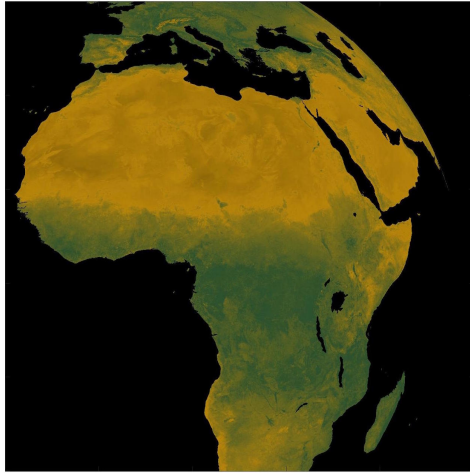


FIG. 15. NDVI with custom colourmap applied.

For a clear validation that the NDVI methodology proposed here is effective, Fig. 16, shows a comparison between an image of Spain and Portugal, taken from Google Earth [9], and a corresponding section of Fig. 15.

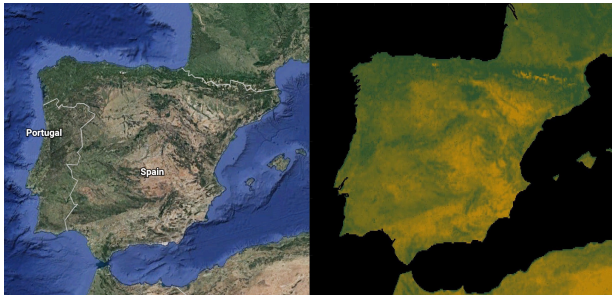


FIG. 16. Comparison between Google Earth satellite image of Spain/Portugal (left) with the corresponding section of the NDVI image (right).

B. The Normalized Difference Snow Index

Another noticeable trait of NDVI calculation is that it returns similar values for snow and desert, due to the similar reflective properties of each terrain. The Pyrenees, for instance, in Fig. 16 and the Alps in Fig. 15 appear as desert. In order to effectively detect snow, another index must be used: the Normalized Difference Snow Index (NDSI). The difference formula used is similar to Eq. 1, and relies on the fact that snow is highly reflective in visible band and highly absorptive in the near-infrared or short-wave infrared band [10]. Hence, the order of the terms in the numerator of Eq. 2 are reversed. Cloud free images in the relevant bands were produced, the pixel values converted to physical radiances using Eq. 2 and the following formula applied

$$NDSI = \frac{R_{0.6\mu m} - R_{12.0\mu m}}{R_{0.6\mu m} + R_{12.0\mu m}} \quad (3)$$

where the subscripts denote the spectral bands selected for this method [1].

Images of the two spectral bands used and the resultant NDSI are presented in Fig. 17.

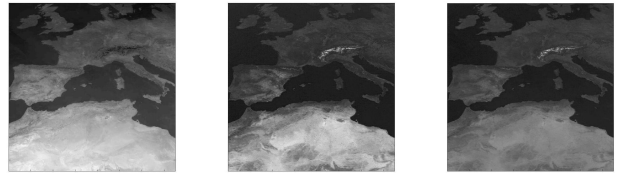


FIG. 17. Comparison of cloud-removed IR $12.0\mu m$ image (left), cloud-removed visible $0.6\mu m$ (center) image, and the resulting NDSI (right).

Here, cloud free images have been used but, since the reflectance of clouds remains high in the selected bands, the NDSI would have still allowed for good separation of most clouds and snow had the input images been cloudy [10].

V. APPLICATIONS OF NDVI/NDSI

Here we explore some applications of NDVI/NDSI and the cloud removal methods we have previously described. First, we perform some quick ‘back-of-the-envelope’ calculations to measure the approximate size of the Sahara Desert and the percentage snow coverage in the Alps and Dolomites. Subsequently, we calculate how the NDVI changes seasonally in Africa, in a more mathematically rigorous framework.

A. Initial Measurements

1. Determining the Size of the Sahara Desert

The Meteosat-8 geostationary satellite provides measurements with a spatial linear resolution of approximately 3km [5]. Therefore, if we know that the physical area represented by one pixel of the NDVI image is approximately equal to 9km^2 , we can count the desert pixels in a particular section of an image and calculate an approximation of the physical area of desert present.



FIG. 18. Rectangular section of the NDVI image centered over the Sahara desert, used for size determination.

Performing this calculation on a rectangular section of the NDVI that encloses the Sahara (shown in Fig. 18) yields a result of $11.5 \text{ million km}^2$, which is accurate to within a 30% tolerance of the actual size of the Sahara desert (approximately 9 million km^2 [11]). This value is an overestimate because, in reality, barren soil and desert terrain exists in this region outside of the boundaries of what we call the Sahara desert. EUMETSAT do not provide the uncertainty on the spatial linear resolution of a single pixel. However, using error propagation laws, we can reverse-calculate that an uncertainty of 0.14km would bring our discrepancy to within 1σ . The most significant source of error here is human: where the value of the threshold between desert and non-desert is set impacts the final result dramatically.

Performing a calculation such as this on a number of NDVI images over a substantial time course (a decade for example) and plotting desert size as a function of time, may be an effective method for quantifying desertification. Likewise, the NDVI data could highlight the effects of deforestation in a particular area over time or act as an indicator of drought [2]. In section VB, NDVI as a function of time is used to analyse the seasonal variation in vegetation in a particular part of Africa.

2. Measuring Alpine Snow Cover

By applying the same methodology as above to a section of an NDSI image centered over the Alps and Dolomites (Fig. 19), the physical area of the Alps and Dolomites that is covered by snow can be determined.

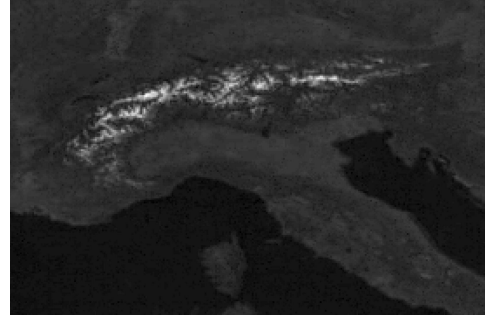


FIG. 19. Rectangular section of the NDSI image centered over the Alps and Dolomites, used for determination of snow cover.

In the image shown in Fig. 19, approximately 9200km^2 of land was determined to be covered by snow, which is equivalent to approximately 3% of the total area of the Alps and Dolomites (approximately 314000km^2 [12]). It is important to note here that this NDSI image has been calculated using two cloud removed spectral band images which themselves have been produced using 86 images taken between March and June 2012 (the only data available for use at the time of this calculation). A more useful snow coverage calculation may involve images taken during the winter months; it is likely that Fig. 19 is mostly just highlighting glacial peaks which have snow cover all year round. It is also noticeable in Fig. 19 that the Apennine mountains do not appear. Since they are much lower than the Alps and Dolomites [13][14], it is expected that they would have little snow cover between March and June. An NDSI image produced from spectral band images during the winter months may allow for detection of snow cover in the Apennines.

As with section VA1, the next avenue to pursue here would be to measure snow coverage as a function of time, perhaps to observe the effects of climate change.

B. Measuring Seasonal Variation in African Vegetation

The NDVI is a powerful tool, not only to calculate the spatial extent of barren/fertile land at a given time, but also to observe fluctuations in vegetation over time. To demonstrate this we selected an area of northern Africa which spans Niger, Nigeria, Chad, Sudan, South Sudan and Cameroon with an area of approximately 1.5 million km^2 . This region is displayed in Fig. 20, selected appropriately from the colour image presented in Fig. 11 and will hereon be referred to as the *ROI* (Region of Interest).

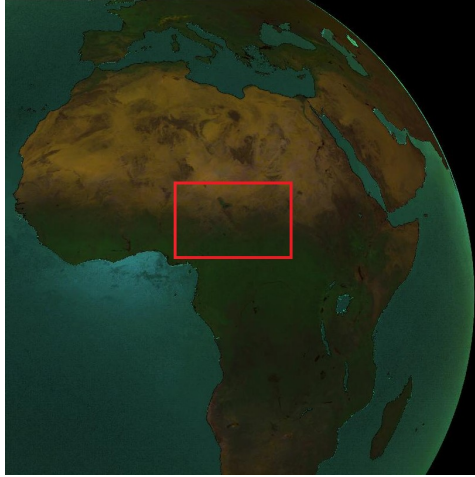


FIG. 20. Highlighted region in central Africa. This region was chosen specifically because of its approximately 50/50 split between barren and fertile land.

We analysed data from 322 days over 2011, in order to observe how the vegetation index varied over time in the *ROI*. In this endeavor, the cloud removal methods presented in Section II were redundant. This is because they are not designed to remove cloud from a specific day, but rather to produce a cloud free image which is representative of a range of many days. Therefore when calculating the NDVI over days in 2011, we required two reference cloudless images (for both visible and IR). The references were simply composite cloud-removed images which were calculated using all 322 images from 2011 for both bands. To detect clouds in the daily images, we calculated the difference between the daily images in the visible and IR bands against their respective reference images. Globally thresholding these difference images accordingly, revealed the clouds effectively. The pixels deemed to be ‘cloudy’ according to the threshold, were screened from all subsequent calculation of NDVI. The non-cloudy pixels were then thresholded according to their NDVI values in much the same way as Fig. 14. A sample of the binarised NDVI images of the *ROI* are displayed in Fig. 21.

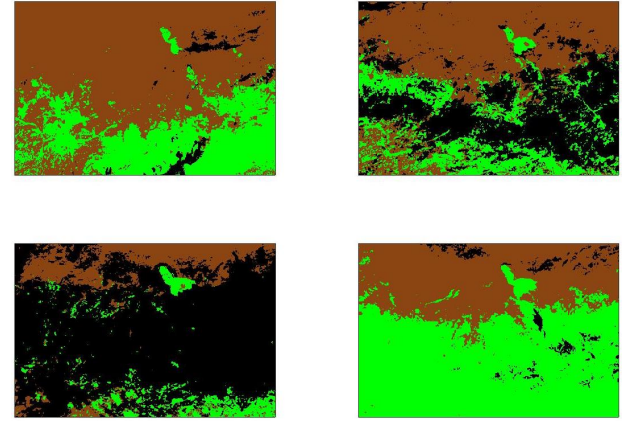


FIG. 21. Binarised NDVI images of the *ROI*, calculated for four single days over various months during 2012. Top left: March. Top Right: December. Bottom Left: June. Bottom Right: August. Here green corresponds to fertile land, brown corresponds to barren land and black corresponds to cloud.

From the data presented in each subset of Fig. 21, it is possible to calculate a fraction of visible fertile land to total visible land. This can be expressed mathematically as

$$F = \frac{N_{green}}{N_{green} + N_{brown}} \quad (4)$$

where F represents the fraction of visible fertile land to total visible land and N represents the number of pixels attributed to a certain colour. For example, the F values calculated for the four images shown in Fig. 21 are 0.30 (March), 0.29 (December), 0.31 (June) and 0.62 (August). By calculating F values over the whole year of 2011, it is possible to observe the fluctuation from green to barren, and back again, over 12 months. We hypothesised that F would fluctuate over the year, peaking in winter when temperatures are coolest, and dipping in summer when temperatures are warmest. This annual fluctuation is presented in Fig. 22.

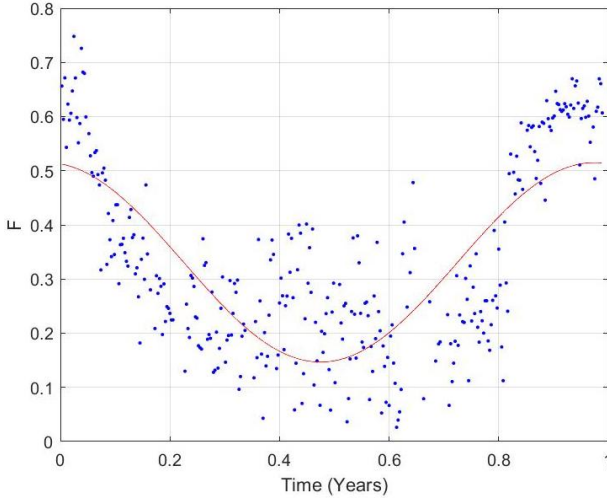


FIG. 22. Scatter plot of F against time, over the year of 2011. The red line is a line of best fit of the form $A\sin(\omega t + B) + C$ where A , B and C are fitted constants.

This approximate sine wave confirmed our hypothesis that the fertility of the region would oscillate with a period of one year. It also confirmed our hypothesis that fertility would peak at the coldest part of the year in the northern hemisphere in January/December time and contrastingly dip during the warmest part of the year June/July.

VI. CONCLUSION

In this report we have explored a wide range of image processing techniques covering cloud removal, constructing colour images and measuring vegetation density and snow coverage. We explored vegetation calculations in further depth, in order to observe seasonal fluctuation at a boundary region between desert and fertile land. It would be interesting in future work to investigate alternative cloud removal techniques (such as those described in Potter and Colman 2003 [1]), especially to formulate a technique which does not involve combining two separate methods, as shown in Fig. 6. This would affect all subsequent calculations which rely on cloud detection/removal, inclusive of all radiance values used in the NDVI calculations. Therefore, utilising an alternative cloud removal technique may produce significantly different NDVI, NDSI and colour image values. Likewise, alternative methods for determining vegetation density, such as the Enhanced Vegetation Index (EVI)[15], may also be of interest.

Given more time to complete this project, we would have acquired more data for different years. This would allow us to observe the seasonal trend in vegetation over years with different global weather patterns, caused by El Niño/La Niña [16]. We would expect that the amplitude of the sinusoidal trend, would be largest for an El Niño year and smallest for a La Niña year.

VII. REFERENCES

- [1] - Potter, T. and Colman, B. (2005). *Handbook of Weather, Climate and Water*. Hoboken: Wiley-Interscience.
- [2] - Earthobservatory.nasa.gov. (2017). *Measuring Vegetation (NDVI and EVI) : Feature Articles*. [online] Available at: https://earthobservatory.nasa.gov/Features/MeasuringVegetation/measuring_vegetation2.php [Accessed 10 Nov. 2017].
- [3] - Ceinsys.com. (2017). Applications of Satellite Imagery and Remote Sensing Data — Ceinsys. [online] Available at: <http://www.ceinsys.com/blog/applications-of-satellite-imagery-remote-sensing-data/> [Accessed 10 Nov. 2017].
- [4] - Eumetsat.int. (2017). *Welcome to EU-METSAT EUMETSAT*. [online] Available at: <https://www.eumetsat.int/website/home/index.html> [Accessed 10 Nov. 2017].
- [5] - Eumetsat.int. (2017). *The 2nd generation Meteosat-8 satellite takes over Meteosat-7 over the Indian Ocean EUMETSAT*. [online] Available at: <https://www.eumetsat.int/website/home/News/DAT363062.html> [Accessed 10 Nov. 2017].
- [6] - Eumetrain.org. (2017). [online] Available at: <http://www.eumetrain.org/IntGuide/PowerPoints/Channels/conversion.ppt> [Accessed 10 Nov. 2017].
- [7] - Earth.app.goo.gl. (2017). Google Earth. [online] Available at: <https://earth.app.goo.gl/hu9y> [Accessed 10 Nov. 2017].
- [8] - File.scirp.org. (2017). [online] Available at: <https://file.scirp.org/pdf/IJG2015013013110745.pdf> [Accessed 10 Nov. 2017].
- [9] - Earth.app.goo.gl. (2017). Google Earth. [online] Available at: <https://earth.app.goo.gl/T99G> [Accessed 10 Nov. 2017].
- [10] - Hall, D. and Riggs, G. (2011). Normalized-Difference Snow Index (NDSI). Encyclopedia of Earth Sciences Series, pp.779-780.
- [11] - Cook, K. and Vizy, E. (2015). Detection and Analysis of an Amplified Warming of the Sahara Desert. Journal of Climate, 28(16), pp.6560-6580.
- [12] - Peakbagger.com. (2017). Cascade Range - Peakbagger.com. [online] Available at: <http://www.peakbagger.com/range.aspx?rid=33> and <http://www.peakbagger.com/range.aspx?rid=3332> [Accessed 10 Nov. 2017].
- [13] - Encyclopedia Britannica. (2017). Apennine Range — mountains, Italy. [online] Available at: <https://www.britannica.com/place/Apennine-Range> [Accessed 10 Nov. 2017].
- [14] - Encyclopedia Britannica. (2017). Alps — mountains, Europe. [online] Available at: <https://www.britannica.com/place/Alps> [Accessed 10 Nov. 2017].

- [15] - Earthobservatory.nasa.gov. (2017). Measuring Vegetation (NDVI and EVI) : Feature Articles. [online] Available at: <https://earthobservatory.nasa.gov/Features/MeasuringVegetation/measuringvegetation4.php> [Accessed 10 Nov. 2017].
- [16] - Kogan, F. (2000). Satellite-Observed Sensitivity of World Land Ecosystems to El Niño/La Niña. *Remote Sensing of Environment*, 74(3), pp.445-462.